Exploring the possibilities of increasing energy density and efficiency in rechargeable batteries

Download this complimentary article collection
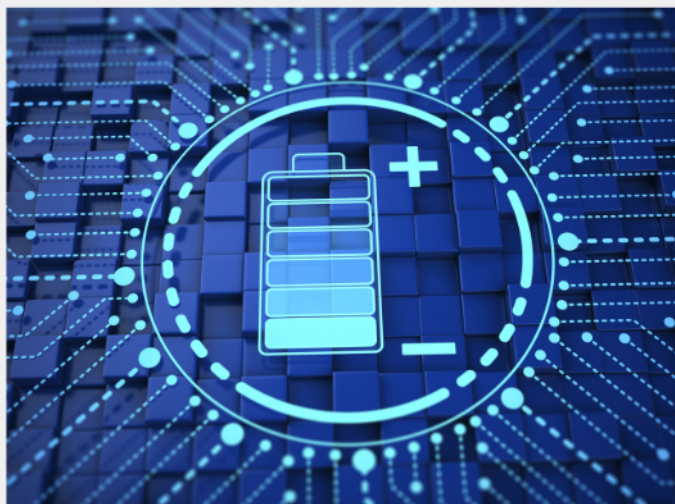
The exponential rise in the need for better, more efficient power sources has sparked an incredible amount of research into batteries. A primary focus of research has been increasing the energy density of batteries, as it allows for lighter, more portable storage of energy. Lithium-ion batteries, for example, have a much higher energy density than conventional lead-acid batteries and can be used for various purposes, such as in electric vehicles.

This article collection provides a comprehensive list of references for new methods and technologies for increasing the energy density of batteries.

Metrohm

WILEY

Comprehensively Strengthened Metal-Oxygen Bonds for Reversible Anionic Redox Reaction

Congcong Cai, Xinyuan Li, Ping Hu, Ting Zhu, Jiantao Li, Hao Fan, Ruohan Yu, Tianyi Zhang, Sungsik Lee, Liang Zhou,* and Liqiang Mai*

Introducing anionic redox in layered oxides is an effective approach to breaking the capacity limit of conventional cationic redox. However, the anionic redox reaction generally suffers from excessive oxidation of lattice oxygen to O_2 and O_2 release, resulting in local structural deterioration and rapid capacity/voltage decay. Here, a $Na_{0.71}Li_{0.22}Al_{0.05}Mn_{0.73}O_2$ (NLAM) cathode material is developed by introducing Al^{3+} into the transition metal (TM) sites. Thanks to the strong Al–O bonding strength and small Al^{3+} radius, the TMO_2 skeleton and the holistic TM–O bonds in NLAM are comprehensively strengthened, which inhibits the excessive lattice oxygen oxidation. The obtained NLAM exhibits a high reversible capacity of 194.4 mAh g^{-1} at 20 mA g^{-1} and decent cyclability with 98.6% capacity retention over 200 cycles at 200 mA g^{-1}. In situ characterizations reveal that the NLAM experiences phase transitions with an intermediate OP4 phase during the charge–discharge. Theoretical calculations further confirm that the Al substitution strategy is beneficial for improving the overlap between Mn 3d and O 2p orbitals. This finding sheds light on the design of layered oxide cathodes with highly reversible anionic redox for sodium storage.

1. Introduction

Sodium-ion batteries (SIBs) are recognized as an effective way to alleviate the resource anxiety of Li-based energy storage devices due to the low-cost and widely distributed Na resource.[1–4]

C. Cai, X. Li, P. Hu, T. Zhu, H. Fan, R. Yu, T. Zhang, L. Zhou, L. Mai
State Key Laboratory of Advanced Technology for Materials Synthesis and Processing
Wuhan University of Technology
Wuhan 430070, P. R. China
E-mail: liangzhou@whut.edu.cn; mlq518@whut.edu.cn
J. Li
Chemical Sciences and Engineering Division
Argonne National Laboratory
9700 South Cass Avenue, Lemont, IL 60439, USA
S. Lee
X-ray Science Division
Argonne National Laboratory
9700 South Cass Avenue, Lemont, IL 60439, USA
L. Zhou, L. Mai
Hubei Longzhong Laboratory
Wuhan University of Technology (Xiangyang Demonstration Zone)
Xiangyang, Hubei 441000, China

The ORCID identification number(s) for the author(s) of this article can be found under https://doi.org/10.1002/adfm.202215155.

DOI: 10.1002/adfm.202215155

However, the widespread application of SIBs is partially hampered by the scarce high-performance cathode materials.[5,6] Layered transition metal oxides (Na_xTMO_2, TM: transition metal) are of increasing interest for their high theoretical capacities and facile 2D Na^+ diffusion channels.[7–9] However, the energy densities of conventional cathode materials are determined by cationic redoxes, mainly TM redoxes, which are approaching the theoretical limits. Recently, the discovery of anionic redox chemistry, especially oxygen redox reaction, inspires new ideas to design high-performance Na_xTMO_2 with high capacities beyond the limit of TM redoxes by triggering the charge transfer of oxygen anions.[10–12]

The oxygen redox reaction has been convincingly demonstrated in Li-rich or Li-excess compounds for lithium-ion batteries. The weak overlap between O 2p and Li 2s orbitals of Li–O–Li configuration leads to the formation of nonbonding O 2p states slightly below the Fermi level (E_f), which will stimulate the oxygen redox reaction.[13,14] A similar situation can be realized in SIBs by constructing Na–O–X configurations, where X can be the alkali metal (Li^+, Na^+),[15–17] alkaline earth metal (Mg^{2+}),[18,19] TM with a full d-shell (Zn^{2+}),[20,21] and even vacancy.[22,23] To achieve high anionic capacity in SIBs, partial substitution of Li^+ into TM layers has received considerable attention.[24,25] As a typical example, Rong et al. designed a P2-type $Na_{0.72}[Li_{0.24}Mn_{0.76}]O_2$ material with a considerable discharge capacity of 270 mAh g^{-1} and an energy density of ≈700 Wh kg^{-1}.[26] Although developing cathode materials with anionic redox reactions represents an effective approach to boosting the capacity, the reversibility of oxygen redox remains a great challenge. Excessive lattice oxygen oxidation can result in irreversible oxygen release. In addition, the lattice oxygen loss will adversely affect the TM redox processes and deteriorate the microstructure.[27–30] As a result, cathode materials with oxygen redox activity generally suffer from oxygen loss and severe capacity/voltage decay over cycling. Enhancing the TM–O bonding strength is the key to overcoming the excessive oxygen oxidation and undesirable irreversibility of anionic redox reaction. As demonstrated previously, introducing high-electronegativity M_e elements (M_e = Cu, Ti, Zr, Sn...) into TM layers to construct strong M_e–O bonds is a conventional way to suppress excessive oxygen oxidation.[31–35]

**ADVANCED
SCIENCE NEWS**

www.advancedsciencenews.com

**ADVANCED
FUNCTIONAL
MATERIALS**

www.afm-journal.de

Although the strong M_e–O bonds have an inhibitory effect on local excessive oxygen oxidation, the large radius of M_e may weaken the holistic TM–O bonding strength. In this regard, searching for a new optimization strategy to comprehensively strengthen the integral TM–O bonding strength is urgently desirable.

In this work, we developed a $Na_{0.71}Li_{0.22}Al_{0.05}Mn_{0.73}O_2$ (NLAM) cathode material. Thanks to the substitution of Mn^{3+} (0.645 Å) sites with small-radius Al^{3+} (0.535 Å) and strong Al–O bonding strength, the TM–O bonds in NLAM have been comprehensively strengthened, and thus the excessive lattice oxygen oxidation is effectively inhibited. The obtained NLAM demonstrates a high reversible capacity of 194.4 mAh g^{-1} at 20 mA g^{-1} within 2.0–4.5 V and a competitive energy density of 534.8 Wh kg^{-1}. What's more, the NLAM manifests decent cyclability with 98.6% capacity retention over 200 cycles at 200 mA g^{-1}. The structural evolution during sodiation/de-sodiation processes is explored by in situ X-ray diffraction (XRD) and Raman. In situ differential electrochemical mass spectrometry (DEMS) and theoretical calculations further confirm the effectively inhibited O_2 generation and improved structural stability in NLAM. This contribution demonstrates an effective approach to boosting the anionic redox activity of layered oxides by comprehensively strengthening TM–O bonds, which sheds light on constructing stable high-energy-density layered oxides with anionic redox for SIBs.

2. Results and Discussion

Enhancing TM–O bonding strength is an effective approach to preventing excessive oxygen oxidation, which is generally dependent on the foreign Metal–O covalency and the ionic radius. To well illustrate the advantages of Al^{3+} substitution, the M–O bonding energy and ionic radius of the candidate elements are shown in Figure S1 (Supporting Information). The Al^{3+} exhibits a high Al–O bonding energy and an impressively small ionic radius among the candidate elements. The former indicates that the Al^{3+} will form strong chemical bonds with the O^{2-} and the latter is beneficial for reducing the TMO_2 layer thickness and enhancing the integral TM–O bonding strength.

The $Na_{0.71}Li_{0.22}Al_xMn_{0.78-x}O_2$ (x = 0, 0.05, 0.1) samples are prepared by a facile solid-state reaction. The structural information of the obtained samples is characterized by XRD. Rietveld refinement patterns of NLM and NLAM are shown in **Figure 1**a,b. Both the NLM and NLAM can be well indexed to the hexagonal P2 phase with a space group of $P63/mmc$. An additional peak at 20.9° can be observed for NLM, implying the honeycomb-ordering superlattice of Li and Mn ions in the TMO_2 layer.[36] However, this peak disappears in the NLAM, suggesting that the successful introduction of Al^{3+} into TM layers disrupts the Li/Mn ordering arrangement. Figure 1c compares the lattice parameters of NLM and NLAM, which are obtained from the Rietveld refinement results (Tables S1 and S2, Supporting Information). Thanks to the smaller ionic radius of Al^{3+} than Mn^{3+} and stronger Al–O bonding strength than Mn–O, the NLAM exhibits decreased TM layer thickness ($d_{(O-TM-O)}$) and increased Na layer thickness ($d_{(O-Na-O)}$) than the NLM, implying the strengthened TMO_2 skeleton and broadened Na$^+$ diffusion

paths. The average TM–O bond length ($d_{(TM-O)}$) of NLAM is calculated to be 1.940 Å, which is obviously shorter than that of NLM (1.960 Å). According to previous understandings,[31] the strengthened TM–O bond would effectively prevent excessive oxygen oxidation and facilitate the reversible anionic redox reaction. When the Al content increases to 10%, impurities can be observed (Figure S2, Supporting Information).

The morphological features of NLM and NLAM are investigated by scanning electron microscopy (SEM) and transmission electron microscopy (TEM). The NLAM is mainly composed of thick flake-like particles, while the NLM exhibits an ellipsoidal shape (Figure S3, Supporting Information). Both samples have an overall particle size of ≈2 µm. Both the NLAM and NLM show solid micron-sized crystals in TEM images (Figure 1d; Figure S4, Supporting Information). Selected-area electron diffraction (SAED) patterns of NLM and NLAM show hexagonally arranged diffraction spots with six-fold symmetry, corresponding to the [001] zone axis of hexagonal lattice (Figure S5, Supporting Information). Sub-spots can be noticed in the SAED pattern of NLM, which further confirms the existence of superlattice structure, agreeing well with the XRD results. High-angle annular dark-field scanning transmission electron microscopy (HAADF-STEM) is employed to further study the atomic structure of NLAM. The high-resolution HAADF-STEM images (Figure 1e,f) further confirm the P2 structure of NLAM, and the measured distance between adjacent layers is ≈5.5 Å. The energy-dispersive spectroscopy (EDS) elemental mapping in Figure 1g demonstrates that all the elements are evenly distributed in NLAM.

X-ray photoelectron spectroscopy (XPS) provides information on the elemental valence states (Figure S6, Supporting Information). For NLM, the Mn $2p_{3/2}$ and Mn $2p_{1/2}$ components are located at ≈642 and 654 eV, respectively. With the introduction of Al^{3+}, the Mn 2p XPS peaks of NLAM shift toward higher binding energy. The substitution of Mn^{3+} with Al^{3+} is beneficial for alleviating the Jahn-Teller distortion of Mn^{3+}, as it reduces the Mn^{3+} amount.

The electrochemical performances of NLAM and NLM were investigated in half cells with Na metals as the anodes. Cyclic voltammetry (CV) profiles of NLAM and NLM are displayed in **Figure 2**a and Figure S7 (Supporting Information). For NLAM, a sharp anionic peak above 3.8 V is observed, corresponding to the continuous anionic oxidation process and the surface passivation of cathode particles during charging. The peaks below 2.5 V are ascribed to the Mn^{3+}/Mn^{4+} redox and the peaks at ≈2.7 V are associated with the Mn^{3+}/Mn^{4+} redox-induced structural ordering transitions during sodiation/de-sodiation. The well-overlapped CV curves beside the first cycle confirm the highly reversible anionic and cationic redox processes. In comparison, the peak related to anionic redox of NLM is above 4.0 V, and this peak suffers from rapid decay during cycling (Figure S7, Supporting Information). The irreversibility may be associated with the lattice oxygen loss and O_2 release.

Representative charge/discharge profiles of NLAM and NLM are displayed in Figure 2b,c. For both NLAM and NLM, the initial charge capacities are mainly contributed from the long slope region above 4.0 V, which corresponds to the anionic redox process.[26] Upon subsequent discharging, the NLAM delivers a high capacity of 194.4 mAh g^{-1} at 20 mA g^{-1} and a high energy density
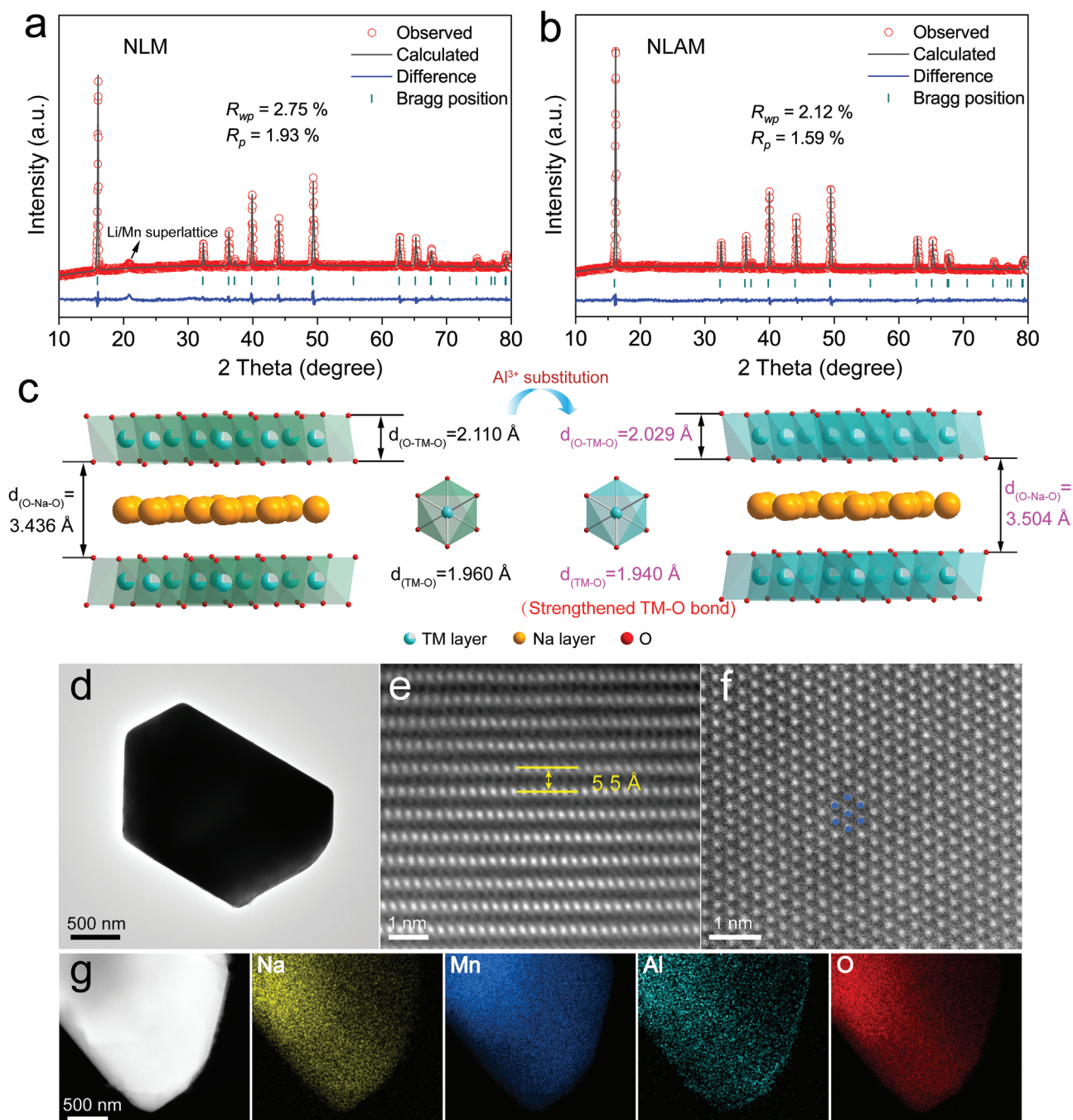
Figure 1. XRD Rietveld refinement of a) NLM and b) NLAM; (c) schematic illustration of the lattice parameter changes upon Al substitution; d) TEM, e,f) high-resolution HAADF-STEM images, and g) EDS-mappings of NLAM.

of 534.8 Wh kg^{-1}. During the following cycles, the NLAM exhibits a highly reversible sodium storage process with ideal capacity retention. Compared to the NLAM, the NLM exhibits a comparable initial discharge capacity (194.3 mAh g^{-1}) at 20 mA g^{-1}. However, the slope region from anionic redox shows a sharp decrease during subsequent charges, suggesting poor reversibility. In addition, the discharge capacity and voltage of NLM also exhibit rapid decay upon cycling. After 20 cycles, the reversible capacity of NLM is only 148.2 mAh g^{-1}, significantly lower

than that of NLAM (193.8 mAh g^{-1}). To further compare the reversibility of anionic redox reaction, the charge capacities above 4.0 V at different cycles are displayed in Figure S8 (Supporting Information), and the NLAM demonstrates obviously enhanced anionic redox capacity retention.

The cycling performances of NLAM and NLM at 50 mA g^{-1} are compared in Figure 2d. After 100 cycles, the NLAM manifests a superior capacity retention of 98.7% with only 0.013% capacity decay per cycle. In sharp contrast, the NLM exhibits a
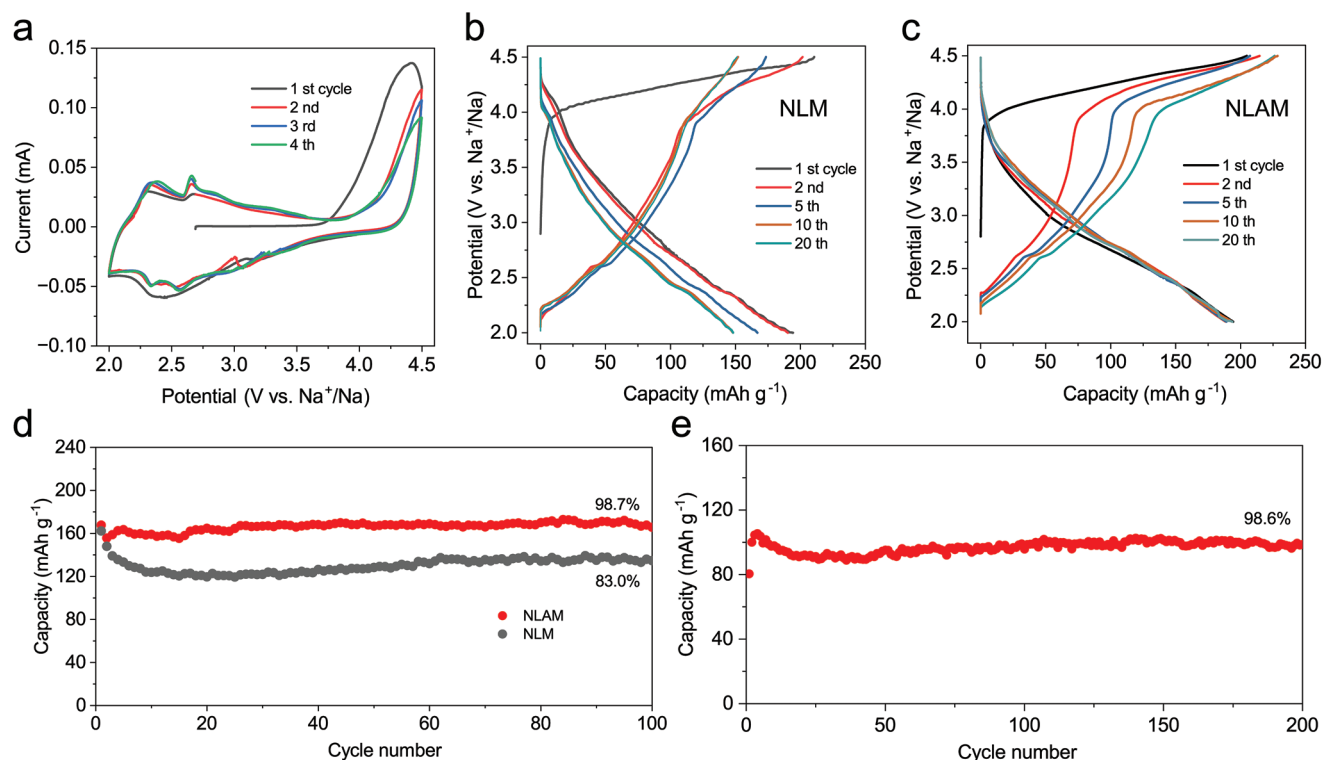
Figure 2. a) The first four CV curves of NLAM collected at 0.1 mV s⁻¹ within the potential range of 2.0–4.5 V versus Na⁺/Na; representative charge/discharge profiles of b) NLM and c) NLAM at 20 mA g⁻¹; d) cycling performances of NLM and NLAM at 50 mA g⁻¹; e) cycling performance of NLAM at 200 mA g⁻¹.

capacity retention of 83% with 0.17% capacity decay per cycle. At 200 mA g⁻¹, the NLAM demonstrates a high capacity retention of 98.6% over 200 cycles (Figure 2e), which exceeds most anionic redox-based cathode materials (Table S3, Supporting Information). The rate performances for NLAM and NLM are presented in Figure S9 (Supporting Information). In general, the NLAM and NLM exhibit similar capacities at different current densities.

To explore the specific influence of Al³⁺ substitution on structural evolution during sodiation/de-sodiation, in situ XRD measurements are employed (**Figure 3**a,b; Figure S10, Supporting Information). For NLM, the (002) and (004) diffractions gradually shift to lower angles during the initial charge process, corresponding to the expansion of lattice parameter *c*. The enlarged interlayer spacing is caused by the increased electrostatic repulsion with the extraction of Na⁺. Meanwhile,
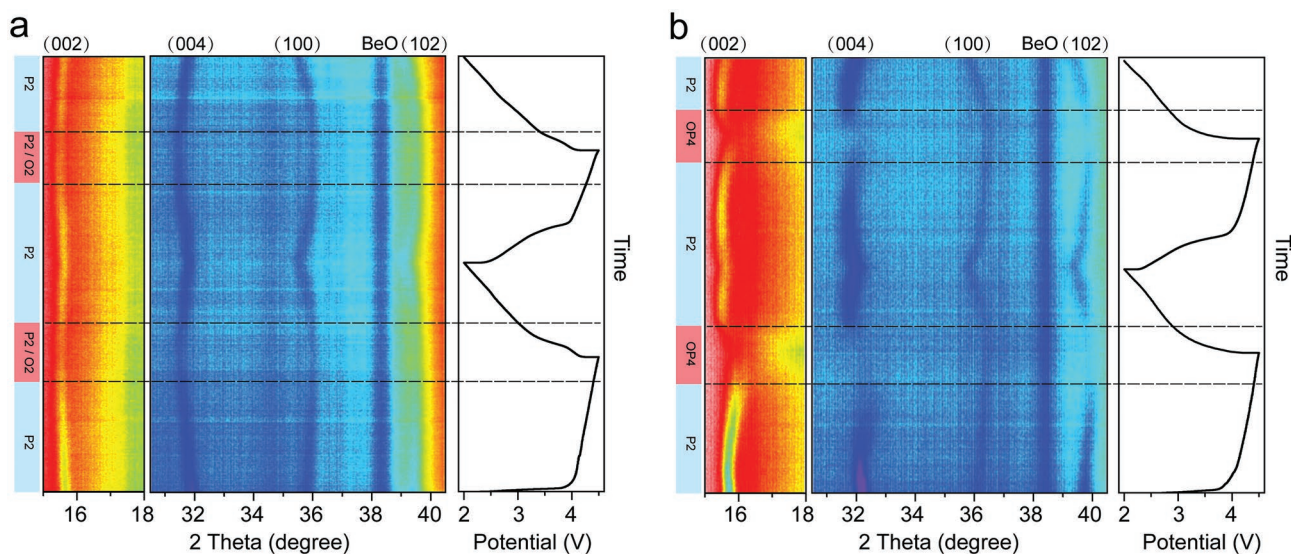
Figure 3. In situ XRD patterns of a) NLM and b) NLAM during the first two cycles.

ADVANCED
SCIENCE NEWS
www.advancedsciencenews.com

ADVANCED
FUNCTIONAL
MATERIALS
www.afm-journal.de

the (100) peak shifts toward a higher angle, which is caused by the shrinkage of lattice parameters *a*. Notably, when charged to over 4.3 V, the (002)$_{P2}$ peak of NLM obviously weakens, which can be ascribed to the formation of O2-type stacking faults at the deep de-sodiation state.[24,37] During discharging, these peaks shift back. The same changes can be observed in the second cycle. The NLAM displays a phase transition behavior different from that of NLM. During the initial charge, the (002) and (004) diffractions shift to lower angles, similar to those of NLM. Meanwhile, the (100) and (102) diffractions shift toward higher angles, suggesting a solid solution reaction. When charged to over 4.3 V, the (002) and (004) diffractions become broad and shift toward higher angles with a P2 to OP4 phase transition. Upon further de-sodiation, the (002)$_{P2}$ peak disappears and transforms into a new (004)$_{OP4}$ diffraction at the end of first charge. The OP4 phase transforms back to the P2 phase during the following discharge process. The same changes also occur in the second cycle, demonstrating the ideal reversibility of NLAM. Through the above analysis, it is

concluded that the P2 phase and O2 stacking faults co-exist at the deep de-sodiation state of NLM. In comparison, the reversible structural evolution of NLAM is enabled by the presence of a stable OP4 phase, which is considered as an intermediate phase for the evolution from P2 to O2 phase. The appearance of this intermediate phase improves the structural integrity by bypassing the sudden transformation from P2 to O2 phase.[24,37]

In situ Raman is further employed to clarify the microstructural evolution of NLAM during de-sodiation/sodiation (**Figure 4**a). The NLAM exhibits three major Raman bands. The peak at ≈646.9 cm^{-1} is assigned to the symmetric stretching vibration (A$_{1g}$) of TM–O bond of layered oxides.[38,39] The bands at ≈600 and ≈498.3 cm^{-1} are assigned to the E$_{2g}$ modes involving both Na and O vibrations, which are associated with the atomic displacements along the *c* axis and parallel to *a*–*b* plane, respectively.[40,41] During the initial charge, the E$_{2g}$ band at ≈600 cm^{-1} presents a redshift to ≈575 cm^{-1} with decreased intensity, which is caused by the Na$^+$ extraction-induced interlayer expansion. The band at ≈498.3 cm^{-1} shifts to higher wavenumbers, which
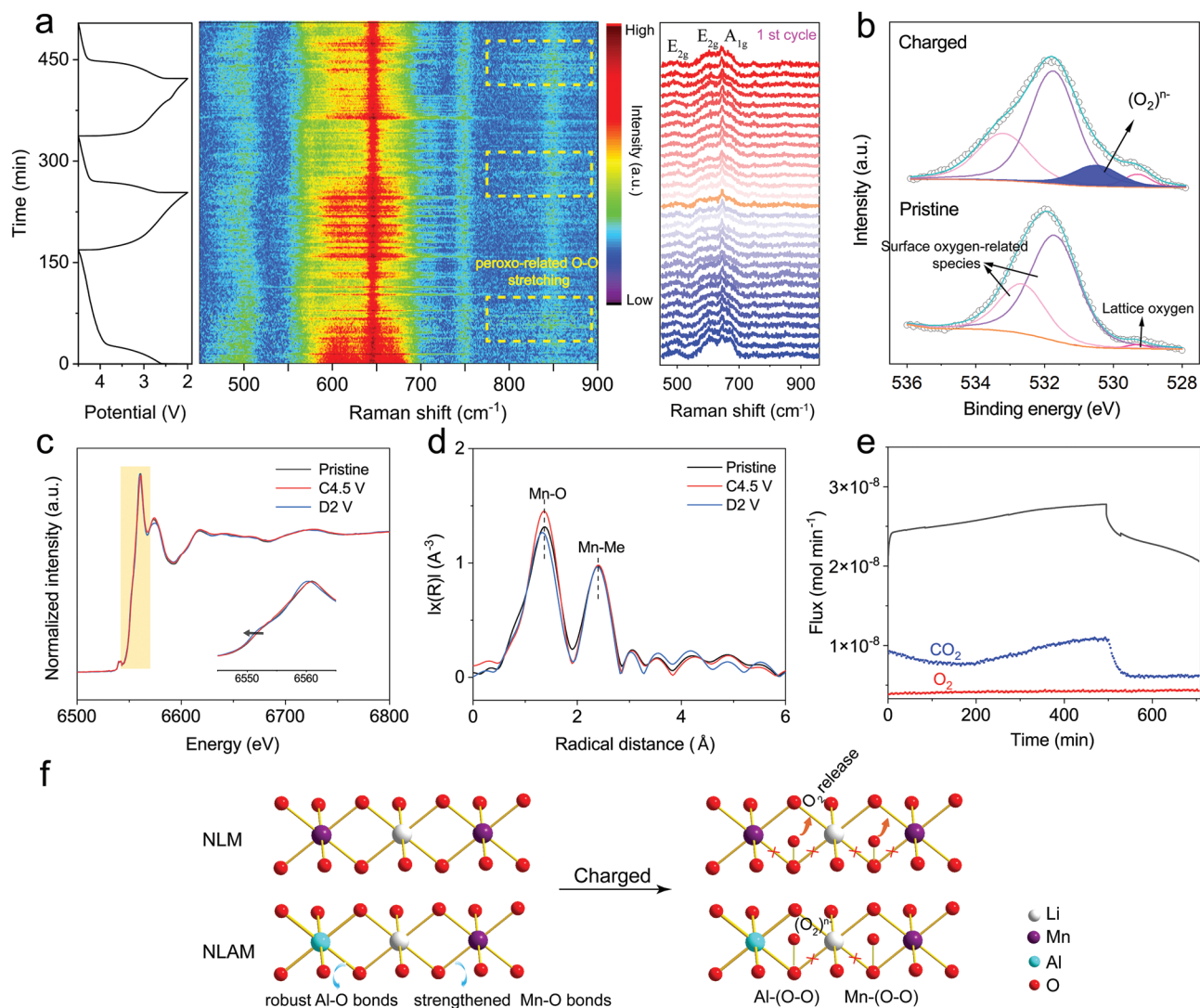
Figure 4. a) In situ Raman spectra and the spectra during the first cycle; b) ex situ O 1s XPS spectra; ex situ Mn *K*-edge c) XANES and d) EXAFS spectra; e) in situ DEMS test of NLAM; f) schematic illustration for the optimized anionic redox reaction mechanism of NLAM.

ADVANCED
SCIENCE NEWS

www.advancedsciencenews.com

ADVANCED
FUNCTIONAL
MATERIALS

www.afm-journal.de

is associated with the shrinkage along the a- and b- axes. Simultaneously, the A_{1g} band narrows, suggesting the distortion of MnO_6 octahedra due to an anionic redox reaction. The E_{2g} band at ≈ 575 cm^{-1} disappears at the fully charged state. Such a change in structure and symmetry is caused by the transformation from P2 to OP4 phase.[38] During discharging, the E_{2g} band reappears and returns to the pristine position accompanied by the broadening of A_{1g} band, indicating the good reversibility of NLAM. Such changes are also observed in the subsequent cycles. Besides, a peak at ≈ 850 cm^{-1} from the peroxo-related O–O stretching appears during the first charge and experiences periodical broadening/narrowing during cycling, which is related to the reversible oxygen redox reactions.[42,43]

The galvanostatic intermittent titration technique (GITT) test at the second cycle is employed to compare the Na$^+$ diffusion coefficients (D_{Na^+}) of NLM and NLAM (Figure S12, Supporting Information). At the beginning of the second charge, the NLAM possesses a slightly higher D_{Na^+} than the NLM due to its larger Na layer thickness. With further charging to higher potentials, the D_{Na^+} of NLAM decreases dramatically due to the P2–OP4 phase transition. Considering the D_{Na^+}, it is reasonable that the NLAM just shows a slight improvement in rate performance when compared to NLM.

To obtain more insight into the anionic redox behavior, ex situ XPS is performed to characterize the electronic structure of oxygen at different sodiation/de-sodiation states, and the O 1s XPS spectra of the NLAM are displayed in Figure 4b. The pristine O 1s spectrum can be deconvoluted into three components. The components at 531.7 and 532.6 eV are assigned to the surface oxygen-related species and the component at 529.3 eV corresponds to the lattice oxygen. After being charged to 4.5 V, an extra component at 530.5 eV appears, which is associated with the intermediate peroxo-like $(O_2)^{n-}$ species from oxygen oxidation.[21] The appearance of $(O_2)^{n-}$ confirms the occurrence of anionic redox reactions.

To further clarify the electronic structure and local environment of NLAM, ex situ X-ray absorption near-edge spectroscopy (XANES) measurements are performed. The Mn K-edge XANES spectra of the pristine state, fully charged state (C4.5 V), and discharged state (D2 V) are displayed in Figure 4c. After initial charging to 4.5 V, the Mn K-edge XANES spectrum does not show an obvious shift, demonstrating that the tetravalent Mn can't be further oxidized and the charge compensation during charging is mainly realized by oxygen oxidation. Upon discharging to 2.0 V, the enlarged Mn K-edge XANES peak shows a slight shift to lower energy, indicating the reduction of Mn to a lower valence state. Figure 4d presents the extended X-ray absorption fine structure (EXAFS) spectra to show the local coordination environment of Mn. The Fourier transformation of EXAFS in Figure 4d features two dominant peaks associated with the Mn–O bond and Mn–M$_e$ (mainly Mn, Al, Li) interaction. The Mn–O distance shows insignificant change during charging, indicating the robust Mn–O bonds. After discharge to 2.0 V, the Mn–O distance decreases slightly, which may be caused by the decrease of ordering degree due to the formation of Mn^{3+}.[34] And the Mn–M$_e$ interaction shows negligible change during charge–discharge.

Excessive lattice oxygen oxidation in Li-doped Na$_x$TMO$_2$ is a common phenomenon, which causes O$_2$ release easily.[33,44–46] To confirm the effective suppression of excessive O^{2-} oxidation

in NLAM, in situ DEMS is conducted to monitor the gas production during charge/discharge. Upon charging, the evolution of CO$_2$ can be clearly detected and its amount reaches the maximum at the end of charge (Figure 4e), which is associated with the decomposition of Na$_2$CO$_3$ in cathode electrolyte interface and oxidation of electrolyte at high voltage.[18] No obvious O$_2$ evolution has been detected during the entire charge/discharge processes, even when fully charged to 4.5 V, indicating the excessive O^{2-} oxidation has been effectively suppressed. The DEMS results further demonstrate the highly reversible anionic redox process in NLAM.

Based on the above discussions, the optimized anionic redox reaction mechanism of NLAM has been proposed (Figure 4f). For NLAM, the introduced Al^{3+} ions preferentially replace the Mn^{3+} sites in the TM layer of NLM due to the same valence state. Thanks to the smaller ionic radius of Al^{3+} compared to that of Mn^{3+} and the strong Al–O bond, the total TM–O bonds in NLAM have been significantly strengthened than those in NLM. Due to the weak bonding of the Na–O–Li configuration, the oxygen redox activity is triggered during the charging process. For NLM, the weak Mn–O bonds are easily broken as the charging process proceeds, resulting in the excessive oxidation of O^{2-} to O$_2$ gas and O$_2$ release. The irreversible anionic redox deteriorates the structure stability. In contrast, the strong Al–O bonds and strengthened Mn–O bonds in NLAM can fix the active oxygen anions in the forms of highly covalent Al–(O–O) and Mn–(O–O) bonds, which prevents the O$_2$ gas release and facilitates the reversibility of O$^{2-}/(O_2)^{n-}$ redox. Benefiting from the highly reversible anionic redox reaction, the NLAM exhibits a high specific capacity with stable cycling stability.

To confirm the effects of Al^{3+} substitution on structure and oxygen redox stability, density functional theory (DFT) calculations are conducted. The optimized models of Na$_{13}$Li$_4$Mn$_{14}$O$_{36}$ (NLM) and Na$_{13}$Li$_4$Mn$_{13}$AlO$_{36}$ (NLAM) are used for simplification (Figure S13, Supporting Information). The density of states (DOS) calculations of NLM and NLAM are displayed in **Figure 5**a,b. A large proportion of isolated O 2p orbital lies slightly below the E_f in both NLM and NLAM, suggesting their oxygen redox activity. The active oxygen state derived from the Na–O–Li configuration will contribute to the charge compensation during electrochemical reaction. In contrast to NLM, the O 2p orbital of NLAM exhibits an elevated energy level toward E_f, indicating that the oxygen redox reactions of NLAM can be triggered at a lower voltage. In addition, the Mn 3d band of NLAM will form bonds in a wider range (Figure 5c), which can improve the involvement of transition metal and oxygen, in favor of reducing the possibility of O$_2$ release. As schematically illustrated in Figure 5d, the NLAM exhibits an elevated O 2p band and an increased overlap between the Mn 3d and O 2p bands than NLM, which is responsible for the higher oxygen redox activity and enhanced structural integrity (Figure 5d).

To visualize more clearly the TM–O covalency, the crystal orbital Hamilton populations (COHP) analysis is employed to provide chemical bonding information (Figure 5e,f). The bond strength denoted by integrated COHP (ICOHP) displays that the NLAM exhibits increased average Mn–O bond strength compared to NLM and strong Al–O bond, indicating the comprehensively strengthened metal-oxygen bonds. The COHP results agree well with the DOS and experimental results.
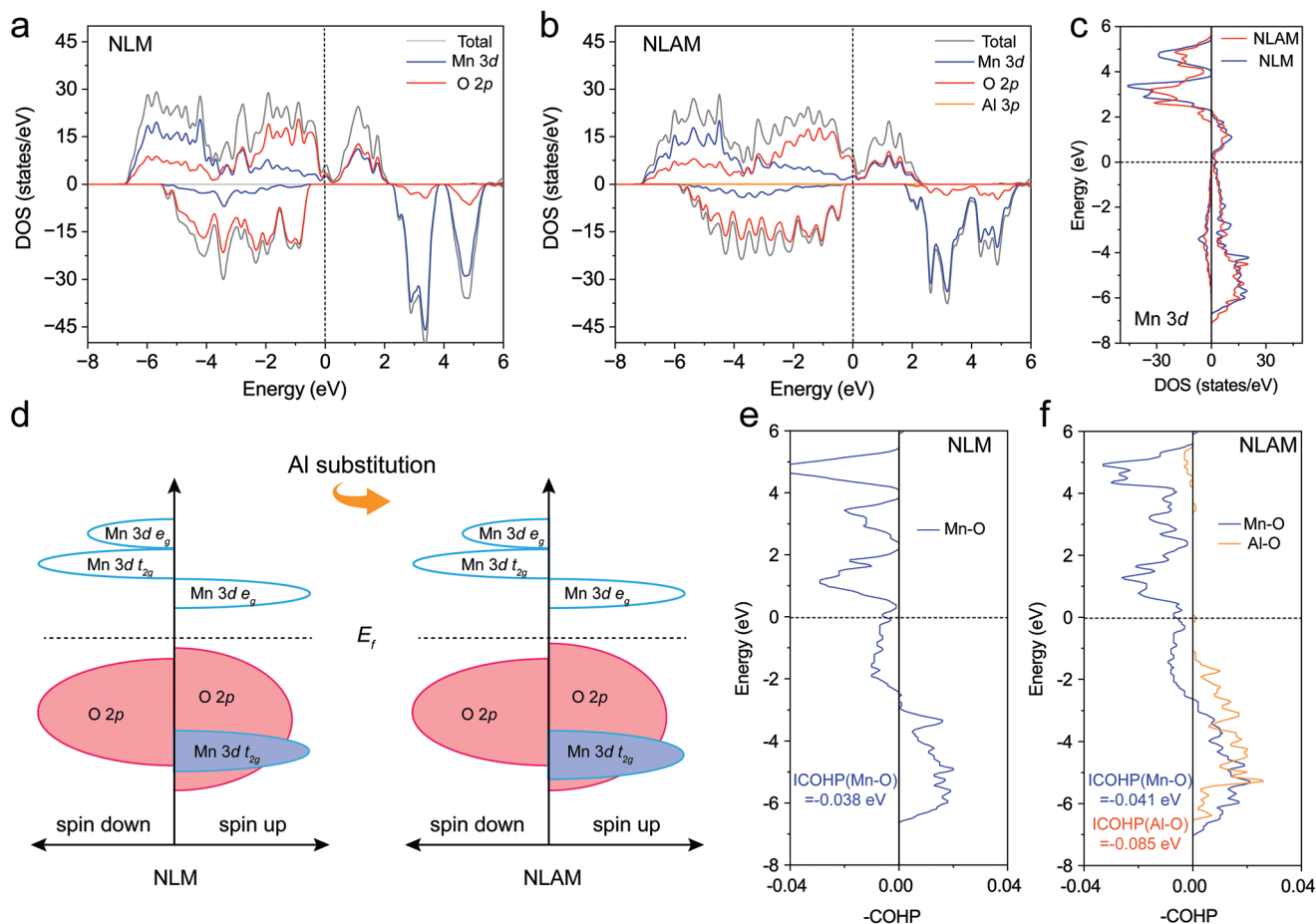
Figure 5. DOS calculations of a) NLM and b) NLAM; c) DOS comparison of Mn 3d orbitals; d) schematic illustration of DOS for NLM and NLAM; COHP calculations of e) NLM and f) NLAM.

3. Conclusion

In summary, we developed an effective strategy to comprehensively enhance the total TM–O bonding strength by Al substitution. Benefited from the strong Al–O bonding strength and small Al^{3+} radius, the obtained $Na_{0.71}Li_{0.22}Al_{0.05}Mn_{0.73}O_2$ (NLAM) exhibits decreased TM layer thickness ($d_{(O-TM-O)}$) and increased Na layer thickness ($d_{(O-Na-O)}$) compared to NLM, leading to a strengthened TMO_2 skeleton and broadened Na^+ diffusion path. The average TM–O bond length ($d_{(TM-O)}$) of NLAM is obviously shorter than that of NLM, suggesting the comprehensively strengthened TM–O bonds of the former. The obtained NLAM demonstrates a high capacity of 194.4 mAh g^{-1} at 20 mA g^{-1} and a competitive energy density of 534.8 Wh kg^{-1}. What's more, the NLAM demonstrates a decent cyclability with 98.6% capacity retention over 200 cycles at 200 mA g^{-1}, demonstrating the highly reversible anionic redox reaction. The structural evolution during sodiation/de-sodiation is explored by in situ XRD/Raman, and ex situ XANES. In situ DEMS and DFT calculations further confirm the effectively inhibited O_2 generation and improved structural stability of NLAM. This study develops an effective approach to improving the anionic redox reversibility through comprehensively strengthening the TM–O bonds, which will shed light on constructing stable high-energy layered oxide cathode materials for SIBs.

Supporting Information

Supporting Information is available from the Wiley Online Library or from the author.

Conflict of Interest

The authors declare no conflict of interest.

Data Availability Statement

The data that support the findings of this study are available from the corresponding author upon reasonable request.

Keywords

[1] N. Yabuuchi, K. Kubota, M. Dahbi, S. Komaba, *Chem. Rev.* **2014**, *114*, 11636.

[2] S. Chen, C. Wu, L. Shen, C. Zhu, Y. Huang, K. Xi, J. Maier, Y. Yu, *Adv. Mater.* **2017**, *29*, 1700431.

[3] N. Yabuuchi, M. Kajiyama, J. Iwatate, H. Nishikawa, S. Hitomi, R. Okuyama, R. Usui, Y. Yamada, S. Komaba, *Nat. Mater.* **2012**, *11*, 512.

[4] C. Cai, Y. Chen, P. Hu, T. Zhu, X. Li, Q. Yu, L. Zhou, X. Yang, L. Mai, *Small* **2022**, *18*, 2105303.

[5] C. Cai, P. Hu, T. Zhu, C. Chen, G. Hu, Z. Liu, Y. Tian, Q. Chen, L. Zhou, L. Mai, *J. Phys. Energy* **2020**, *2*, 025003.

[6] F. Ding, C. Zhao, D. Xiao, X. Rong, H. Wang, Y. Li, Y. Yang, Y. Lu, Y. S. Hu, *J. Am. Chem. Soc.* **2022**, *144*, 8286.

[7] C. Zhao, Q. Wang, Z. Yao, J. Wang, B. Sánchez-Lengeling, F. Ding, X. Qi, Y. Lu, X. Bai, B. Li, H. Li, A. Aspuru-Guzik, X. Huang, C. Delmas, M. Wagemaker, L. Chen, Y.-S. Hu, *Science* **2020**, *370*, 708.

[8] J. Y. Hwang, S. T. Myung, Y. K. Sun, *Chem. Soc. Rev.* **2017**, *46*, 3529.

[9] W. Zuo, X. Liu, J. Qiu, D. Zhang, Z. Xiao, J. Xie, F. Ren, J. Wang, Y. Li, G. F. Ortiz, W. Wen, S. Wu, M. S. Wang, R. Fu, Y. Yang, *Nat. Commun.* **2021**, *12*, 4903.

[10] Q. Liu, Z. Hu, W. Li, C. Zou, H. Jin, S. Wang, S. Chou, S.-X. Dou, *Energy Environ. Sci.* **2021**, *14*, 158.

[11] H. Xu, S. Guo, H. Zhou, *J. Mater. Chem. A* **2019**, *7*, 23662.

[12] Q. Shen, Y. Liu, L. Jiao, X. Qu, J. Chen, *Energy Storage Mater.* **2021**, *35*, 400.

[13] H. Ren, Y. Li, Q. Ni, Y. Bai, H. Zhao, C. Wu, *Adv. Mater.* **2022**, *34*, 2106171.

[14] D.-H. Seo, J. Lee, A. Urban, R. Malik, S. Kang, G. Ceder, *Nat. Chem* **2016**, *8*, 692.

[15] X. Rong, J. Liu, E. Hu, Y. Liu, Y. Wang, J. Wu, X. Yu, K. Page, Y.-S. Hu, W. Yang, H. Li, X.-Q. Yang, L. Chen, X. Huang, *Joule* **2018**, *2*, 125.

[16] B. Mortemard de Boisse, M. Reynaud, J. Ma, J. Kikkawa, S. I. Nishimura, M. Casas-Cabanas, C. Delmas, M. Okubo, A. Yamada, *Nat. Commun.* **2019**, *10*, 2185.

[17] X. Zhang, Y. Qiao, S. Guo, K. Jiang, S. Xu, H. Xu, P. Wang, P. He, H. Zhou, *Adv. Mater.* **2019**, *31*, 1807770.

[18] U. Maitra, R. A. House, J. W. Somerville, N. Tapia-Ruiz, J. G. Lozano, N. Guerrini, R. Hao, K. Luo, L. Jin, M. A. Perez-Osorio, F. Massel, D. M. Pickup, S. Ramos, X. Lu, D. E. McNally, A. V. Chadwick, F. Giustino, T. Schmitt, L. C. Duda, M. R. Roberts, P. G. Bruce, *Nat. Chem.* **2018**, *10*, 288.

[19] K. Dai, J. Wu, Z. Zhuo, Q. Li, S. Sallis, J. Mao, G. Ai, C. Sun, Z. Li, W. E. Gent, W. C. Chueh, Y. Chuang, R. Zeng, Z. Shen, F. Pan, S. Yan, L. Piper, Z. Hussain, G. Liu, W. Yang, *Joule* **2019**, *3*, 518.

[20] A. Konarov, J. H. Jo, J. U. Choi, Z. Bakenov, H. Yashiro, J. Kim, S.-T. Myung, *Nano Energy* **2019**, *59*, 197.

[21] X. Bai, M. Sathiya, B. Mendoza-Sánchez, A. Iadecola, J. Vergnet, R. Dedryvère, M. Saubanère, A. M. Abakumov, P. Rozier, J.-M. Tarascon, *Adv. Energy Mater.* **2018**, *8*, 1802379.

[22] B. Song, M. Tang, E. Hu, O. J. Borkiewicz, K. M. Wiaderek, Y. Zhang, N. D. Phillip, X. Liu, Z. Shadike, C. Li, L. Song, Y.-Y. Hu, M. Chi, G. M. Veith, X.-Q. Yang, J. Liu, J. Nanda, K. Page, A. Huq, *Chem. Mater.* **2019**, *31*, 3756.

[23] C. Zhao, Q. Wang, Y. Lu, L. Jiang, L. Liu, X. Yu, L. Chen, B. Li, Y.-S. Hu, *Energy Storage Mater.* **2019**, *20*, 395.

[24] N. Voronina, M. Y. Shin, H. J. Kim, N. Yaqoob, O. Guillon, S. H. Song, H. Kim, H. D. Lim, H. G. Jung, Y. Kim, H. K. Lee, K. S. Lee, K. Yazawa, K. Gotoh, P. Kaghazchi, S. T. Myung, *Adv. Energy Mater.* **2022**, *12*, 2103939.

[25] G. H. Yoon, S. Koo, S. J. Park, J. Lee, C. Koo, S. H. Song, T. Y. Jeon, H. Kim, J. S. Bae, W. J. Moon, S. P. Cho, D. Kim, S. H. Yu, *Adv. Energy Mater.* **2022**, *12*, 2103384.

[26] X. Rong, E. Hu, Y. Lu, F. Meng, C. Zhao, X. Wang, Q. Zhang, X. Yu, L. Gu, Y.-S. Hu, H. Li, X. Huang, X.-Q Yang, C. Delmas, L. Chen, *Joule* **2019**, *3*, 503.

[27] E. McCalla, M. T. Sougrati, G. Rousse, E. J. Berg, A. Abakumov, N. Recham, K. Ramesha, M. Sathiya, R. Dominko, G. Van Tendeloo, P. Novak, J. M. Tarascon, *J. Am. Chem. Soc.* **2015**, *137*, 4804.

[28] X. D. Zhang, J. L. Shi, J. Y. Liang, Y. X. Yin, J. N. Zhang, X. Q. Yu, Y. G. Guo, *Adv. Mater.* **2018**, *30*, 1801751.

[29] S. Y. Kim, C. S. Park, S. Hosseini, J. Lampert, Y. J. Kim, L. F. Nazar, *Adv. Energy Mater.* **2021**, *11*, 2100552.

[30] L. Mu, R. Lin, R. Xu, L. Han, S. Xia, D. Sokaras, J. D. Steiner, T. C. Weng, D. Nordlund, M. M. Doeff, Y. Liu, K. Zhao, H. L. Xin, F. Lin, *Nano Lett.* **2018**, *18*, 3241.

[31] P.-F. Wang, Y. Xiao, N. Piao, Q.-C. Wang, X. Ji, T. Jin, Y.-J. Guo, S. Liu, T. Deng, C. Cui, L. Chen, Y.-G. Guo, X.-Q. Yang, C. Wang, *Nano Energy* **2020**, *69*, 104474.

[32] C. Cheng, C. Chen, S. Chu, H. Hu, T. Yan, X. Xia, X. Feng, J. Guo, D. Sun, J. Wu, S. Guo, L. Zhang, *Adv. Mater.* **2022**, *34*, 2201152.

[33] X. Cao, X. Li, Y. Qiao, M. Jia, F. Qiu, Y. He, P. He, H. Zhou, *ACS Energy Lett.* **2019**, *4*, 2409.

[34] H. Xu, C. Cheng, S. Chu, X. Zhang, J. Wu, L. Zhang, S. Guo, H. Zhou, *Adv. Funct. Mater.* **2020**, *30*, 2005164.

[35] C. Zhao, C. Li, Q. Yang, Q. Qiu, W. Tong, S. Zheng, J. Ma, M. Shen, B. Hu, *Energy Storage Mater.* **2021**, *39*, 60.

[36] R. A. House, U. Maitra, M. A. Perez-Osorio, J. G. Lozano, L. Jin, J. W. Somerville, L. C. Duda, A. Nag, A. Walters, K. J. Zhou, M. R. Roberts, P. G. Bruce, *Nature* **2020**, *577*, 502.

[37] J. W. Somerville, A. Sobkowiak, N. Tapia-Ruiz, J. Billaud, J. G. Lozano, R. A. House, L. C. Gallington, T. Ericsson, L. Häggström, M. R. Roberts, U. Maitra, P. G. Bruce, *Energy Environ. Sci.* **2019**, *12*, 2223.

[38] G. Singh, J. M. López del Amo, M. Galceran, S. Pérez-Villar, T. Rojo, *J. Mater. Chem. A* **2015**, *3*, 6954.

[39] D. Eum, B. Kim, J. H. Song, H. Park, H. Y. Jang, S. J. Kim, S. P. Cho, M. H. Lee, J. H. Heo, J. Park, Y. Ko, S. K. Park, J. Kim, K. Oh, D. H. Kim, S. J. Kang, K. Kang, *Nat. Mater.* **2022**, *21*, 664.

[40] Y. G. Shi, Y. L. Liu, H. X. Yang, C. J. Nie, R. Jin, J. Q. Li, *Phys. Rev. B* **2004**, *70*, 052502.

[41] N. Jiang, Q. Liu, J. Wang, W. Yang, W. Ma, L. Zhang, Z. Peng, Z. Zhang, *Small* **2021**, *17*, 2007103.

[42] X. Cao, H. Li, Y. Qiao, X. Li, M. Jia, J. Cabana, H. Zhou, *Adv. Energy Mater.* **2020**, *10*, 1903785.

[43] X. Cao, H. Li, Y. Qiao, M. Jia, X. Li, J. Cabana, H. Zhou, *Adv. Mater.* **2021**, *33*, 2004280.

[44] X. Chen, N. Li, E. Kedzie, B. D. McCloskey, H. Tang, W. Tong, *J. Electrochem. Soc.* **2019**, *166*, A4136.

[45] C. Zhao, Q. Yang, F. Geng, C. Li, N. Zhang, J. Ma, W. Tong, B. Hu, *ACS Appl. Mater. Interf.* **2020**, *13*, 360.

[46] X. Qi, L. Wu, Z. Li, Y. Xiang, Y. Liu, K. Huang, E. Yuval, D. Aurbach, X. Zhang, *Adv. Energy Mater.* **2022**, *12*, 2202355.